NIH Public Access
Author Manuscript
NMR Biomed. Author manuscript; available in PMC 2013 June 18.

Published in final edited form as:
NMR Biomed. 2011 August ; 24(7): 855–864. doi:10.1002/nbm.1631.

Quantifying cortical bone water *in vivo* by three-dimensional ultra-short echo-time MRI

Hamidreza Saligheh Rad[a], **Shing Chun Benny Lam**[a], **Jeremy F. Magland**[a], **Henry Ong**[a], **Cheng Li**[a], **Hee Kwon Song**[a], **James Love**[a], and **Felix W. Wehrli**[a,*]

[a]Laboratory for Structural NMR Imaging, Department of Radiology, University of Pennsylvania School of Medicine, Philadelphia, PA, USA

Abstract

Bone contains a significant fraction of water that is not detectable with ordinary Cartesian imaging sequences. The advent of ultra-short echo-time (UTE) methods has allowed the recovery of this submillisecond T_2^* water. In this work, we have developed a new three-dimensional hybrid-radial ultra-short echo-time (3D HRUTE) imaging technique based on slab selection by means of half-sinc pulses, variable-TE slice encoding and algorithms for quantification. The protocol consists of collecting two datasets differing in TR, from which T_1 is extracted, which is needed for quantification. Unlike T_2^*, which has been found to vary within a narrow range and does not require individual correction, T_1 is critically subject dependent (range, 100–350 ms). No soft-tissue suppression was used to preserve the signal-to-noise ratio of the short-T_2 bone water protons or to minimize the loss of relatively mobile water in large pores. Critical for quantification is correction for spatial variations in reception field and selection of the endosteal boundary for inclusion of pixels in the bone water calculation, because of the ruffled boundary stemming from trabecularization of the endosteal surface. The reproducibility, evaluated in 10 subjects covering the age range 30–80 years, yielded an average coefficient of variation of 4.2% and an intraclass correlation coefficient of 0.95, suggesting that a treatment effect on the order of 5% could be detected in as few as 10 subjects. Lastly, experiments in specimens by means of graded deuterium exchange showed that approximately 90% of the detected signal arises from water protons, whose relaxation rates ($1/T_1$ and $1/T_2^*$) scale linearly with the isotopic volume fraction of light water after stepwise exchange with heavy water. The data thus show conclusively that the method quantifies water even though, *in vivo*, no distinction can be made between various fractions, such as collagen-bound *vs* pore-resident water.

Keywords

three-dimensional ultra-short echo-time MRI; bone water; cortical bone; deuterium exchange

INTRODUCTION

The mechanical competence of cortical bone is a function of both composition and architecture at the macro- and microstructural levels (1). The fracture resistance of cortical bone is adversely affected by the age-related increase in cortical porosity, which is aggravated in osteoporosis. Although increased porosity results in decreased areal or volumetric bone mineral density (BMD), the majority of pores are below the resolution limit

Copyright © 2011 John Wiley & Sons, Ltd.

*Correspondence to: F. W. Wehrli, University of Pennsylvania School of Medicine, 1 Founders, MRI Education Center, 3400 Spruce Street, Philadelphia, PA 19104, USA. wehrli@mail.med.upenn.edu.

NIH-PA Author Manuscript
NIH-PA Author Manuscript
NIH-PA Author Manuscript

NIH-PA Author Manuscript

NIH-PA Author Manuscript

NIH-PA Author Manuscript

achievable *in vivo*. Therefore, an increase in pore volume in the presence of normally mineralized bone cannot be distinguished from the situation in which the pore volume is unaltered but the bone is undermineralized as, for example, in osteomalacia. However, there is no broad consensus that the intrinsic mechanical properties of osteoporotic bone are substantially different from those of normal bone. Rather, the impaired strength of osteoporotic cortical bone is a consequence of the increased pore volume fraction (2).

The spaces of the Haversian and lacuno-canalicular system making up the total pore volume are filled with fluid, essentially consisting of water (3). Hence, a knowledge of the bone water (BW) content would provide some measure of pore volume fraction [even though a substantial fraction of the detected water is associated with the collagen matrix (4)]. As the surface interactions of water confined to the tight spaces of these pores cause the lifetime of the water signal to be extremely short ($T_2^* < 1$ ms), solid-state imaging techniques are required for its capture.

In 2003, Robson *et al.* (5) described what they referred to as ultra-short echo-time (UTE) imaging, a two-dimensional imaging technique using radial acquisition of the free induction decay in conjunction with half-sinc pulses and various approaches for the suppression of long-T_2 components. They showed that, in conjunction with ramp sampling, they could sample the center of *k* space in less than 100 μs after excitation, thereby capturing the signal from protons not ordinarily detected, including the protons in cortical bone. Subsequent work conducted at 1.5 T suggested that the proton signal in human cortical bone at the mid-tibia had a lifetime on the order of 400–500 μs (6), commensurate with a linewidth of 0.6–0.7 kHz. Fernandez *et al.* (7) found the majority of the proton spectrum measured at 9.4 T *ex vivo* in rabbit cortical bone to have a linewidth of about 1.2 kHz. Further, the signal amplitude was attenuated by about 90% on immersion in D_2O, suggesting that it originated predominantly from water (7). This exchange behavior was later confirmed in human bone by Techawiboonwong *et al.* (8), who found a residual signal on the order of 15% on complete exchange in sheep cortical bone.

A different acquisition strategy was pursued by Wu *et al.* (9) based on three-dimensional radial sampling of the free induction decay in the presence of a short, 10-μs, rectangular radiofrequency (RF) pulse [instead of slice-selective, half-sinc pulses of several hundred microseconds in duration, as in refs. (5,6,10)] applied in the presence of the readout gradient. The resulting signal is therefore likely to contain contributions from the organic matrix, rather than just water in various binding states. This group of workers subsequently perfected the method, together with a technique for the suppression of water and fat signal (termed WASPI), for the quantification of the matrix volume and, in conjunction with quantitative ^{31}P imaging of the bone's mineral constituents, yielding a measure of the mineralization density (4,11).

Previously, some of the present authors conceived and implemented a two-dimensional UTE method for the quantifi-cation of proton density in cortical bone, as a possible surrogate for bone porosity (8,10). This recent work has shown promise as a technique to characterize bone disease, including osteoporosis and renal osteodystrophy. Unlike WASPI, which is based on very short (~10 μs) hard pulses, the present method does not detect protons that are part of the collagen matrix [with T_2^* on the order of 10–20 μs (7)], as these are not amenable to slice-selective, half-sinc pulse excitation. Instead, it aims to detect and quantify signals from protons with linewidths on the order of 1 kHz, previously suggested to arise mainly from water. The objective of the present work was to further develop and investigate a new three-dimensional hybrid-radial ultra-short echo-time (3D HRUTE) pulse sequence that minimizes the various possible analysis and measurement errors and provides a better slice profile with less out-of-slice excitation than in two-dimensional UTE (12). We show

NIH-PA Author Manuscript

NIH-PA Author Manuscript

NIH-PA Author Manuscript

that the quantification process is sensitive to various sources of systematic and random errors, including nonideal behavior of the imaging gradients affecting the reconstruction of ramp-sampled *k* space, and mismatch of signals from paired acquisitions with opposite polarity of the excitation gradient. We further show that a knowledge of T_1 is essential for quantification, which is achieved by the incorporation of T_1 quantification into HRUTE. We describe an acquisition and analysis protocol and evaluate the various sources of systematic errors. Finally, we evaluate the origin of the UTE proton signal on specimens of lamb tibia cortical bone after graded exchange with D_2O.

MATERIALS AND METHODS

Summary of approach

The quantification of water proton density in cortical bone by *in vivo* MRI can be performed by comparing the proton signal in the bone against the signal in a reference sample with known concentration values; through a conditioning process, as shown previously (8):

$$\rho_{\text{bone}}=\rho_{\text{ref}}(I_{\text{bone}}F_{\text{ref}})/(I_{\text{ref}}F_{\text{bone}})\cdot\exp(-\text{TE}_{\text{eff}}(R_{2\text{ref}}{}^{*}-R_{2\text{bone}}{}^{*})) \quad [1]$$

where ρ_{bone} and ρ_{ref} are the volumetric proton densities of the bone and reference sample, respectively, and I_{bone} and I_{ref} are the measured image intensities in bone and the reference sample, respectively. Here, we chose as reference sample 20% H_2O in D_2O doped with 27 mM $MnCl_2$, yielding T_1 ~ 15 ms and T_2^* ~ 320 μs. $R_{2\text{bone}}{}^{*}$ and $R_{2\text{ref}}{}^{*}$ are the effective transverse relaxation rates ($R_2^* = 1/T_2^*$) for bone ($T_{2\text{bone}}{}^{*}$ ~ 750 μs) and the reference sample ($T_{2\text{ref}}{}^{*}$ ~ 320 μs), respectively, and TE_{eff} is the effective echo-time. The relative signal amplitudes F_{ref} and F_{bone} are functions of the relaxation times, pulse repetition time TR and, as the pulse duration τ is of the same order or longer than T_2^*, the ratios $\tau/T_{2\text{bone}}{}^{*}$ and $\tau/T_{2\text{ref}}{}^{*}$. By expressing the normalized longitudinal and transverse magnetization immediately after the RF pulse as $f_z(\tau/T_2^*)$ and $f_{xy}(\tau/T_2^*)$, we can express F as:

$$\begin{aligned} F&=f(T_1,T_2^*,\tau,\text{TR})\\ &=f_{xy}(\tau/T_2^*)\cdot(1-\exp(-\text{TR}/T_1))/(1-f_z(\tau/T_2^*)\cdot\exp(-\text{TR}/T_1)) \end{aligned} \quad [2]$$

Although, for rectangular RF pulses, analytical expressions have been derived for $f_{xy}(\tau/T_2^*)$ and $f_z(\tau/T_2^*)$ (13), for shaped pulses these parameters must be calculated numerically.

Data acquisition, reconstruction and quantification

MRI pulse sequence—The three-dimensional acquisition strategy chosen has potential advantages over two-dimensional UTE for the target application. First, the three-dimensional technique allows the computation of a spatial average of bone water concentration [BWC(*x,y,z*)] from multiple slices, thereby minimizing random and systematic errors, including acquisition noise, segmentation error and registration errors. Moreover, it reduces measurement errors, such as finding the location of the measurement site. Second, the considerably shorter T_1 of BW compared with tissue water (200–400 ms *vs* ~1500 ms for muscle, for example, at 3 T) favors a three-dimensional technique over multi-slice two-dimensional acquisition by avoiding harmful T_1 recovery effects, whilst, at the same time, providing a superior slice profile with less out-of-slice excitation. Third, it is not known to what extent BWC is spatially variant (e.g. along the shaft of long bones); therefore, efficient acquisition of a larger number of slices is potentially advantageous for the systematic study of these spatial variations.

NIH-PA Author Manuscript

NIH-PA Author Manuscript

NIH-PA Author Manuscript

Figure 1a shows the diagram of the proposed 3D HRUTE sequence designed to acquire images from the cortical bone with or without soft-tissue suppression. Sample images obtained with the two options are given in Figure 1b, c. The sequence employs selective excitation half-sinc pulses (14) to excite a 5.0-cm axial slab, corresponding to a half-sinc pulse with a main-lobe duration of about 160 μs and a gradient strength of 2.9 mT/m, in order to acquire 10 evaluable 4.5-mm axial slices for the quantification process [total of 20 slices at a field of view (FOV_z) of 90 mm]. Hybrid encoding is achieved via radial readout with ramp sampling on the k_x–k_y plane and Fourier encoding along k_z. To minimize the signal loss from T_2^* decay during the phase-encoding period, the duration of the trapezoidal gradients is stepped, thereby minimizing TE at $k_z = 0$ (15,16). Optional long-T_2 suppression is achieved using spectrally selective dual-band pulses introduced in ref. (17). These pulses are more robust to off-resonance than long rectangular pulses (13) without introducing T_1 selectivity or compromising short-T_2 signal levels. In addition, they are able to include long-T_2 suppression at both the water and fat resonances, as they excite spins located at both water and fat frequencies. For measurements *in vivo*, the excitation slab was centered at 38% of the tibia length, known to be the site of maximum cortical thickness (18), measured from the medial malleolus.

All imaging was performed at 3 T (Siemens Tim Trio, Erlangen, Germany), with an eight-channel transmit–receive knee coil, using the following parameters: FOV, 180 × 180 mm^2; 500 radial projections; 256 readout samples; dwell time, 6 μs ($Bandwidth_{readout}$ = 325 Hz/pixel); TR = 20 ms; reconstructed pixel size, 0.38 × 0.38 mm^2; flip angle, 23° (corresponding to the Ernst angle for an average T_1 of 250 ms); total scan time, 6.6 min. In order to ensure proper readout of the data, the receiver was opened 30 μs before the gradients were switched on, leading to five dummy acquisition points per readout. Thus, this delay, together with the minimum practical RF-to-readout transition time, yielded TE_{min} = 80 μs at $k_z = 0$. The specific absorption rate was below 2 W/kg.

All water quantification studies were performed without long-T_2 suppression with the rationale being that larger pores are likely to have prolonged T_2, therefore risking suppression of these resulting signals. Further, long-T_2 suppression leads to partial suppression of BW signals, thereby complicating quantification, as the degree of suppression depends on individual pixel T_2^*, which is unknown.

Regridding and image reconstruction—*k*-space data were regridded and three-dimensional Fourier reconstructed off-line using custom-designed software programmed in MATLAB (Version 7.5, MathWorks, Natick, MA, USA). After inverse fast Fourier transformation of the three-dimensional *k*-space data along k_z, each two-dimensional hybrid k_x-k_y dataset underwent three steps to yield a set of two-dimensional images for each slice along *z*: (i) weighting of the data using Voronoi weights; (ii) two-dimensional regridding of type II [method of Greengard and Lee (19)]; and (iii) two-dimensional inverse fast Fourier transformation.

Gradient mapping—The regridding process needs to have precise information on the *k*-space trajectories, which are functions of the performance of the readout gradients. Therefore, the regridding process of the radial *k*-space sampled data, unlike Cartesian-based acquisition methods, is highly susceptible to small timing errors and nonideal *k*-space trajectories caused by deviations of the actual from nominal readout gradients at locations of rapid temporal changes in amplitude, such as near vertices of trapezoidal waveforms. Various strategies have been used to measure such delays (20,21).

As the above effects are scanner hardware specific, a one-time mapping of the *k*-space trajectories was performed during ramp-up by directly measuring the *k*-space trajectory,

NIH-PA Author Manuscript

NIH-PA Author Manuscript

NIH-PA Author Manuscript

yielding the actual shape of the ramp-up portion of the readout gradients, as well as gradient delays. These timings were adjusted prospectively in the reconstruction code (22).

RF coil inhomogeneity correction—Quantification is based on image intensity comparison between a tissue location and a partially separate location of a reference sample. Therefore, even minor inhomogeneities of the transmit field or spatial dependence of the receive coil sensitivity can introduce large systematic errors. The human subject studies were carried out with an extremity quadrature bird-cage transmit–eight-channel receive coil (Invivo Corp., Orlando, FL, USA), which required some correction for inhomogeneity in the received signal. Typically, both three-dimensional receive and three-dimensional transmit B_1 mapping are necessary to compensate for these inhomogeneities. Transmit B_1 variations across the imaging volume were found to be within ±5% of the nominal value, as determined using the actual flip-angle imaging technique (23), therefore obviating the need for correction. The effects from an inhomogeneous reception profile were corrected by creating a mask with the aid of a homogeneous phantom and dividing the bone intensity image by the mask, pixel by pixel. Figure 2a illustrates the principle, employing reference samples consisting of 20% H_2O in D_2O doped with 27 mM $MnCl_2$ (T_1 ~ 15 ms and T_2^* ~ 320 μs). Further, in order to minimize errors from receive coil inhomogeneity along the coil's axis, the coil was carefully positioned at the tibia's 38% location coincident with the magnet iso-center. Before measuring the signals S_{bone} and S_{ref}, images were intensity normalized (Figure 2b).

Cortical bone segmentation—To facilitate large-scale processing of the image data, an automatic algorithm was developed and implemented in MATLAB (Version 7.5, MathWorks) to segment the cortical bone region (24). In this algorithm, the three-dimensional stack of images was first denoised with an anisotropic diffusion filter (25). Thereafter, in each two-dimensional slice, the cortical bone region was segmented via region growing (26) and detection of the peaks of the first derivative of the intensity profile at each degree after polar image transform, as illustrated in Figure 3. The algorithm is designed such that two user-selectable parameters for both endosteal and periosteal boundaries can be chosen, essentially allowing the placement of the inner and outer segmentation boundaries by a given number of pixels from the actual detected boundary. The parameters denoted *marginIn* and *marginOut* determine how much of the cortex is included in the parameter computation. As shown later, it is particularly *marginIn* that critically affects the quantification results of BWC (and T_1).

T_1 and T_2^* mapping—Previous work has shown that BW T_1 is subject dependent, increasing with increasing porosity (8). Hence, the efficient quantification of T_1 is essential for the method to be practical. As shown in eqns [1] and [2], the derived BWC (ρ_{bone}) is strongly dependent on T_1. Therefore, T_1 mapping was incorporated into the 3D HRUTE imaging protocol, based on the concatenation of two sequences differing in TR, with TR_1 = 20 ms and TR_2 = 60 ms. T_1 was then computed from the intensity ratio, $r = S_1/S_2$, by numerically solving the nonlinear equation:

$$r = \frac{1-\exp(-\mathrm{TR}_1/T_1)}{1-f_z\exp(-\mathrm{TR}_1/T_1)} \Big/ \frac{1-\exp(-\mathrm{TR}_2/T_1)}{1-F_z\exp(-\mathrm{TR}_2/T_1)} \quad [3]$$

which is solved via inverse optimization. In the equation, the imaging parameters (flip angle, RF pulse shape, TR_1, TR_2) are known and T_{1ref}, T_{2ref}^* and T_{2bone}^* are measured or can be estimated. Several processing strategies are possible. Although a pixel-wise calculation of T_1 is desirable, it is prone to errors from misregistration between the two images (TR_1 and TR_2) or minor inconsistencies in segmentation. Therefore, averaging was preferred at the stage of the images from which T_1 is calculated (inverse solution to eqn [3]).

NIH-PA Author Manuscript

NIH-PA Author Manuscript

NIH-PA Author Manuscript

In contrast with T_1, previous work has shown that T_2^* in cortical bone *in vivo* varies less with age (6). Further, as TE $\ll T_2^*$, errors are less critical in affecting the accuracy of the derived BWC. To evaluate the range of T_2^* for human subject studies, T_2^* was computed in six subjects, three men and three women, aged 50–80 years. Parametric T_2^* maps were generated from eight echoes obtained by varying TE in steps of 200 μs from 250 to 1650 μs, and fitting the amplitudes to a decaying exponential. Figure 4 illustrates and summarizes different steps of the image analysis and quantification of BWC *in vivo*.

Reproducibility

The reproducibility was evaluated in 10 healthy subjects (five men and five women) covering the age range 30–80 years, representative of the cohort of healthy subjects to be evaluated in a subsequent study, based on the following enrollment criteria: body mass index (BMI) < 30 kg/m^2; BMD z scores (by dual-energy X-ray absorptiometry at both hip and spine), $-2 \leq z \leq 2$. Further, subjects with medical histories that indicated disorders (e.g. malabsorption syndromes, renal or hepatic disease), those who had undergone surgery and those receiving treatments compromising bone mineral homeostasis were excluded. The root-mean-square difference between baseline and repeat was calculated, as well as the intraclass correlation coefficient, as measures of precision and reliability.

Specimen studies

To evaluate the performance of 3D HRUTE acquisition and analysis for BWC quantification via eqn [1], BWC was calculated in cortical bone specimens from lamb tibia after stepwise exchange of native water (H_2O) by deuterium oxide (D_2O) – similar to the approach described by Techawiboonwong *et al.* (8). This approach is based on the concept that the isotopic ratio for exchangeable protons in bone at equilibrium matches that of the immersion fluid. Hence, as the H_2O concentration in bone is varied by a known increment, the intensity of the BW signal, corrected for relaxation, changes by a commensurate fraction.

Lamb shank (tibia), purchased from a local butcher, was cleaned of all soft tissue, including marrow, and cut transversely into three ~ 1.5-cm sections (proximal, central and distal). Specimens were then immersed in mixtures of distilled H_2O and 99.8% D_2O (Sigma-Aldrich, St. Louis, MO, USA) with varying isotopic composition (0%, 20%, 40%, 60%, 80% and 100% H_2O volume fraction) at approximately 1 : 10 bone-to-fluid volume ratio for ~ 72 h at 50°C (to enhance the exchange rate). After equilibration, the isotopic ratio of the exchangeable hydrogen in bone and the immersion mixture should be equal because of the conservation of mass (8). For each isotopic composition, TE was varied in steps of 200 μs from 250 to 2050 μs, and parametric T_2^* maps were calculated. Similarly, T_1 was computed based on the dual-TR sequence and eqn [3], yielding T_1 maps for each isotopic mixture. As T_2^* and HRUTE experiments do not have the same resolution, only average T_2^* values (together with parametric T_1 maps) were used to calculate parametric BWC images via eqn [1].

RESULTS

Human subject studies

Figure 5a, b shows cortical bone images in the mid-shaft tibia in the center for two female subjects differing in age, together with parametric BWC maps superimposed on anatomic images to illustrate the wide range of this parameter. Generally, BWC was found to be spatially inhomogeneous, being higher in the anterior aspect of the tibia, in particular in older subjects (Fig. 5b). In younger subjects, BWC histograms were approximately Gaussian, as in the case of the 33-year-old woman, with variances approximately paralleling their means. In contrast, in older subjects, such as the 64-year-old woman, deviation from

NIH-PA Author Manuscript

NIH-PA Author Manuscript

NIH-PA Author Manuscript

Gaussianity was substantial with a tail towards greater BWC values (Fig. 5c, d). We also noted longer T_1 values with elevated BWC in the older subject, consistent with more porous bone overall, as larger pores are associated with longer T_1 values as they have a lower surface-to-volume ratio [as the relaxation rate increases with the surface-to-volume area (27)].

Figure 6a displays a series of images obtained by incrementing the echo time, showing the exponential decay of the signal over a 2-ms period. Figure 6b shows the parametric T_2^* map superimposed on the anatomic image. Exponential fits to the signal in one pixel and to the average signal over the entire cortical bone area resulted in comparable goodness of fits with $R^2 = 0.99$. The results in this subject suggest that a monoexponential model suffices to explain the transverse relaxation behavior, paralleling earlier observations (6,28). Comparing the T_2^* results derived from two different analysis methods – the average T_2^* from parametric T_2^* maps and T_2^* obtained from fitting average intensities from the entire cortical bone area – yielded good agreement between the two methods, with the mean values not statistically significantly different from each other ($p = 0.19$).

Measurements in six different subjects (see ‘Materials and methods’) yielded an average value of T_2^* of 786 ± 70 μs calculated from averaging the parametric T_2^* map in each subject. There was no trend with age, with an intersubject variation of less than 10%, in agreement with earlier reports (6). Although there is variation in T_2^* within a single subject (see Fig. 6b), we used a T_2^* mean value of 750 μs for the analysis of BWC *in vivo*, as we calculated a spatially averaged BWC as the final result. This is in lieu of the fact that the observed variation in T_2^*, which is on the order of ±25%, only results in BWC deviations of ±5%.

A specific objective in view of future longitudinal studies was the evaluation of reproducibility. Towards this objective, 10 subjects covering the entire age range to be studied were evaluated twice within 2 months. Figure 7 shows a scatter plot of the test–retest data. The results indicate reproducibility with a root-mean-square difference between baseline and repeat of 0.91% BWC or 4.2% relative to the mean value, with an intraclass correlation coefficient of 0.95. This precision would be adequate to detect a treatment effect of 5% with 5% significance and 90% power in 10 subjects.

BWC, T_1 and T_2^* are affected by the choice of pixels included in the segmented cortical bone region. As stated in ‘Materials and methods’, the actual boundary is controlled by two parameters: *marginIn* and *marginOut*. The parameter *marginIn* that controls the endosteal boundary has a more significant effect on BWC quantification because of the fuzzy endosteal boundary caused by trabecularization, particularly prominent in older subjects (29). The phenomenon is illustrated by high-resolution, 3-T, fast large-angle spin-echo (FLASE) images in Fig. 8a, b, clearly showing visible pores at the pixel size used (137 × 137 μm^2). At the lower resolution of HRUTE images, trabeculae are not resolved, but simply give rise to a continuum of varying intensity in the radial direction. Therefore, too small a value of *marginIn* will include a portion of the trabecularized cortex, whereas too large a value may underestimate a significant fraction of the pore volume. Figure 8c, d shows the endosteal boundaries obtained with two different values of *marginIn*. Their estimated BWC and T_1 values were 21.70% and 157 ms, respectively, for *marginIn* = 2, and 18.9% and 137 ms, respectively, for *marginIn* = 4. More research is needed to determine the best value of *marginIn* to specify the optimal cortex area to exclude trabecularized bone. There-fore, we chose *marginIn* = 4 for this study based on a visual inspection of the segmentation results.

NIH-PA Author Manuscript

NIH-PA Author Manuscript

NIH-PA Author Manuscript

Specimen studies

Figure 9a illustrates the imaging set-up with the specimens labeled. Figure 9b displays intensity images for one of the specimens as a function of the volume fraction of H_2O of the immersion fluid, showing decreasing intensity with decreasing proton content. Figure 9c shows the average $1/T_1$ value calculated from the parametric map as a function of isotopic composition, indicating a high degree of linearity. Fits to the data from individual specimens were not statistically significantly different from one another. Therefore, the data were pooled for regression. The 0% H_2O data were excluded from $1/T_1$ and $1/T_2^*$ fits as they do not represent exchangeable protons (note the residual signal in Fig. 9b). A similar linear relationship was observed for the average $1/T_2^*$ value calculated from the parametric map (Fig. 9d). It should also be noted that the signal amplitude values fitted well to a monoexponential model. For example, specimen 1B in 40% H_2O yielded single-pixel fits with $R^2 = 0.999$, and similar results were obtained when average intensities were fitted ($R^2 = 0.997$).

In Fig. 9e, the average BWC for six bone specimens as a function of H_2O fraction is plotted after subtracting a non-exchangeable proton contribution of 2.0% at $[H_2O] = 0$ from all values. The fit of the data to the five concentration values yielded $R^2 = 0.96$ ($p < 0.0001$) with a *y*-intercept of 1.7% BWC. We therefore estimate a total non-exchangeable proton contribution to the apparent BWC values on the order of 2–4%. Relative to the mean value from all six specimens of 26.5 ± 1.6%, there is a fraction on the order of 8–15% that must be attributed to nonexchangeable protons, most probably fat, based on the T_1 value (see above) and the chemical shift reported previously by Fernandez *et al.* (7).

DISCUSSION AND CONCLUSIONS

The data presented in this work suggest that BWC can be measured reliably with good precision, thereby detecting changes during aging or in response to treatment. The proposed algorithm involves the quantification of T_1, which was found to be subject dependent (unlike T_2^*). The approach chosen relies on a three-dimensional hybrid-radial imaging technique based on slab selection by means of half-sinc pulses, and is an extension of the method first demonstrated by Robson *et al.* (5). 3D HRUTE has some advantages over multi-slice techniques, albeit at the expense of increased echo time. This problem, however, is mitigated through the modulation of the duration of the slice-encoding gradient (15,16) (rather than the amplitude as normally). Three-dimensional imaging with slice encoding requires short TR in order to be efficient, which is facilitated by the relatively short T_1 of BW.

In this work, we opted not to use soft-tissue suppression for two reasons. Long-T_2 suppression techniques entail a significant signal-to-noise ratio penalty on the BW protons to be detected. Further, large pores, which occur in older subjects near the endosteal surface as a result of the trabecularization of bone, contain relatively mobile water whose signal would be attenuated significantly by soft-tissue suppression pulses. The downside of not using soft-tissue suppression is the potential inclusion of marrow in the ruffled boundary region, which depends critically on the chosen segmentation boundary. The automatic segmentation algorithm employed to segment out the cortical bone area takes advantage of two user-selectable parameters for endosteal and periosteal boundaries. Apparent BWC and T_1 are likely to be overestimated as the endosteal segmentation boundary is moved inwards. Conversely, too conservative a boundary selection will exclude regions of greater porosity, and thus lead to the underestimation of BWC.

The specimen data match previous results (8), showing that the majority of the UTE proton signal arises from exchangeable protons, and that the calculated proton concentration scales

NIH-PA Author Manuscript

NIH-PA Author Manuscript

NIH-PA Author Manuscript

linearly with the isotopic volume fraction of light water after stepwise exchange with heavy water. Further evidence that the signal arises from water stems from the observation that both the longitudinal and transverse relaxation rates are found to scale linearly with the light water fraction of the immersion medium, consistent with dipole–dipole relaxation as the dominant mechanism of interaction and the much lower magnetic moment of the deuteron.

The linearity of the relaxation rates with increasing proton fraction of the immersion fluid is expected, considering that the mechanism of relaxation is dipole–dipole interaction and that the gyromagnetic ratio γ of the deuteron is lower by a factor of 6.5 than that of the proton because the relaxation rates behave as $1/T_{1,2} \propto \gamma_H^2 \gamma_D^2$. Analogous to previous experiments (7,8), we conclude from these data that the majority of the signal in cortical bone originates from exchangeable protons, and is therefore most probably from water. However, the residual signal after complete exchange is clearly of different origin, yielding a mean T_1 value of 302 ± 45 ms, consistent with methylene protons in fatty acid triglycerides.

Although we continue to refer to the measured proton density converted to the volume fraction of water as ‘bone water’, it is clear from our specimen data, as well as previous work, that there is a fraction of the signal that is of different origin, most probably fatty acid triglyceride. We estimate this fraction to be on the order of 8–15%. Further, recent preliminary work performed by Ong *et al.* (30), using deuterium MR in human cortical bone specimens at 9.4 T, showed that over half of this water is collagen-bound water. However, with advancing age, the pore volume fraction increases relative to that of collagen-bound water. Horch *et al.* (31) used T_2 proton relaxation spectra at 4.7 T obtained by fitting the Carr–Purcell–Meiboom–Gill signal to a range of exponentials. They assigned a fraction of the overall signal, with T_2 on the order of 400 μs, to collagen-bound water and a broad distribution, with T_2 values ranging from a few milliseconds to about 1 s, to pore water.

One of the key goals of this work was to evaluate reproducibility in view of future longitudinal studies, as it has been shown that porosity is at least partially reversible by antiresorptive drug treatment (32). Cortical porosity is also a hallmark of renal dystrophy (8,33), and the condition is likely to be alleviated on kidney transplantation. Hence, the measurement of reproducibility is of interest in that it determines the statistical power. Our data suggest that a treatment effect on the order of 5% could be detected in as few as 10 subjects.

The method currently has several limitations. First, BWC is not equivalent to porosity, as pointed out above, as a significant fraction of the detected water is not water in the Haversian and lacuno-canalicular pore system, but rather collagen-bound, as shown in the recent work discussed above. Neither of the two approaches used in refs. (30,31) is feasible *in vivo*. However, another more practical limitation is the distinction of pore water from marrow in the trabecularized boundary, which requires a judicious choice of segmentation boundary. We have already seen that the apparent BWC is critically dependent on the endosteal boundary chosen. Finally, the present and previous studies have been conducted in the tibial midshaft, which has the advantage of a superficial location and is easily accessible with surface or volume coils. However, the tibial cortex is not a site of fracture, unlike the femoral neck. Nevertheless, cortical porosity is systemic in nature, and age- and disease-related changes have been observed via destructive imaging or histomorphometry *ex vivo* at multiple skeletal locations, including the humerus (34), femoral shaft (35) and femoral neck (36), showing a similar pattern.

NIH-PA Author Manuscript

NIH-PA Author Manuscript

NIH-PA Author Manuscript

Acknowledgments

This work was supported by National Institutes of Health grant R01 AR50068. The authors are grateful to Drs Yusuf Bhagat and Alexander Wright for acquiring and processing the high-resolution images in Fig. 8a, b.

Abbreviations used

BMD	bone mineral density
BMI	body mass index
BW	bone water
BWC	bone water concentration
FLASE	fast large-angle spin-echo
FOV	field of view
RF	radiofrequency
UTE	ultra-short echo-time
WASPI	water- and fat-suppressed proton projection MRI
3D HRUTE	three-dimensional hybrid-radial ultra-short echo-time

References

1. Seeman E, Delmas PD. Bone quality – the material and structural basis of bone strength and fragility. N Engl J Med. 2006; 354(21):2250–2261. [PubMed: 16723616]
2. Wachter NJ, Krischak GD, Mentzel M, Sarkar MR, Ebinger T, Kinzl L, Claes L, Augat P. Correlation of bone mineral density with strength and microstructural parameters of cortical bone in vitro. Bone. 2002; 31(1):90–95. [PubMed: 12110418]
3. Timmins PA, Wall JC. Bone water. Calcif Tissue Res. 1977; 23(1):1–5. [PubMed: 890540]
4. Cao H, Ackerman JL, Hrovat MI, Graham L, Glimcher MJ, Wu Y. Quantitative bone matrix density measurement by water- and fat-suppressed proton projection MRI (WASPI) with polymer calibration phantoms. Magn Reson Med. 2008; 60(6):1433–1443. [PubMed: 19025909]
5. Robson MD, Gatehouse PD, Bydder M, Bydder GM. Magnetic resonance: an introduction to ultrashort TE (UTE) imaging. J Comput Assist Tomogr. 2003; 27(6):825–846. [PubMed: 14600447]
6. Reichert IL, Robson MD, Gatehouse PD, He T, Chappell KE, Holmes J, Girgis S, Bydder GM. Magnetic resonance imaging of cortical bone with ultrashort TE pulse sequences. Magn Reson Imaging. 2005; 23(5):611–618. [PubMed: 16051035]
7. Fernandez-Seara M, Wehrli SL, Takahashi M, Wehrli FW. Water content measured by proton–deuteron exchange NMR predicts bone mineral density and mechanical properties. J Bone Mineral Res. 2004; 19(2):289–296.
8. Techawiboonwong A, Song HK, Leonard MB, Wehrli FW. Cortical bone water: in vivo quantification with ultrashort echo-time MR imaging. Radiology. 2008; 248(3):824–833. [PubMed: 18632530]
9. Wu Y, Ackerman JL, Chesler DA, Graham L, Wang Y, Glimcher MJ. Density of organic matrix of native mineralized bone measured by water- and fat-suppressed proton projection MRI. Magn Reson Med. 2003; 50(1):59–68. [PubMed: 12815679]
10. Techawiboonwong A, Song HK, Wehrli FW. In vivo MRI of submilli-second T(2) species with two-dimensional and three-dimensional radial sequences and applications to the measurement of cortical bone water. NMR Biomed. 2007; 21(1):59–70. [PubMed: 17506113]
11. Cao H, Nazarian A, Ackerman JL, Snyder BD, Rosenberg AE, Nazarian RM, Hrovat MI, Dai G, Mintzopoulos D, Wu Y. Quantitative (31)P NMR spectroscopy and (1)H MRI measurements of

NIH-PA Author Manuscript

NIH-PA Author Manuscript

NIH-PA Author Manuscript

bone mineral and matrix density differentiate metabolic bone diseases in rat models. Bone. 2010; 46(6):1582–1590. [PubMed: 20188225]

12. Josan S, Kaye E, Pauly J, Daniel B, Pauly K. Improved half RF slice selectivity in the presence of eddy currents with out-of-slice saturation. Magn Reson Med. 2009; 61(5):1090–1095. [PubMed: 19319972]
13. Sussman MS, Pauly JM, Wright GA. Design of practical T2-selective RF excitation (TELEX) pulses. Magn Reson Med. 1998; 40(6):890–899. [PubMed: 9840834]
14. Pauly, JM.; Conolly, S.; Nishimura, D.; Macovski, A. A slice-selective excitation for very short T2 species; Proceedings of the 8th Annual Meeting SMRM; Amsterdam, the Netherlands. 1989. p. 28
15. Song HK, Wehrli FW. Variable TE gradient and spin echo sequences for in vivo MR microscopy of short T2 species. Magn Reson Med. 1998; 39:251–258. [PubMed: 9469708]
16. Robson MD, Tyler DJ, Neubauer S. Ultrashort TE chemical shift imaging (UTE-CSI). Magn Reson Med. 2005; 53(2):267–274. [PubMed: 15678544]
17. Larson PE, Gurney PT, Nayak K, Gold GE, Pauly JM, Nishimura DG. Designing long-T2 suppression pulses for ultrashort echo time imaging. Magn Reson Med. 2006; 56(1):94–103. [PubMed: 16724304]
18. Wetzsteon R, Shults J, Zemel B, Gupta PU, Burnham J, Herskovitz R, Howard K, Leonard M. Divergent effects of glucocorticoids on cortical and trabecular compartment bone mineral density in childhood nephrotic syndrome. J Bone Miner Res. 2009; 24:503–513. [PubMed: 19016583]
19. Greengard L, Lee J. Accelerating the nonuniform fast Fourier transform. SIAM Rev. 2004; 46(443):443–454.
20. Peters DC, Derbyshire JA, McVeigh ER. Centering the projection reconstruction trajectory: reducing gradient delay errors. Magn Reson Med. 2003; 50(1):1–6. [PubMed: 12815671]
21. Speier, P.; Trautwein, F. A calibration for radial imaging with large inplane shifts. Proceedings of the 13th Annual Meeting ISMRM; Miami, FL, USA. 2005. p. 2295
22. Magland, J.; Saligheh Rad, H.; Wehrli, FW. Correcting for gradient imperfections in ultra-short echo time imaging. Proceedings of the 18th Annual Meeting ISMRM; Stockholm, Sweden. 2010. p. 3102
23. Yarnykh VL. Actual flip-angle imaging in the pulsed steady state: a method for rapid three-dimensional mapping of the transmitted radiofrequency field. Magn Reson Med. 2007; 57(1):192–200. [PubMed: 17191242]
24. Lam, SCB.; Salilgheh, Rad H.; Magland, J.; Wehrli, FW. Automatic segmentation of MR images for long-bone cross-sectional image analysis. Proceedings of the 18th Annual Meeting ISMRM; Stockholm, Sweden. 2010. p. 3119
25. Perona P, Malik J. Scale-space and edge-detection using anisotropic diffusion. IEEE Trans Pattern Anal Machine Intell. 1990; 12(7):629–639.
26. Gonzalez, RC.; Woods, RE. Digital Image Processing. Prentice Hall; Upper Saddle River, NJ: 2002.
27. Davis CA, Genant HK, Dunham JS. The effects of bone on proton NMR relaxation times of surrrounding liquids. Invest Radiol. 1986; 21:472–477. [PubMed: 3721804]
28. Du, J.; Takahashi, AM.; Carl, M.; Bydder, M.; Szeverenyi, N.; Chung, CB.; Bydder, G. T2 and T1p quantification of cortical bone in vivo using ultrashort TE (UTE) pulse sequences. Proceedings of the 18th Annual Meeting ISMRM; Stockholm, Sweden. 2010. p. 3199
29. Chai B, Tang X, Li H. Osteoclastic resorption of Haversian systems in cortical bone of femoral neck in aged women. A scanning electron microscopic study. Chin Med J (Engl). 1996; 109(9): 705–710. [PubMed: 9275340]
30. Ong, HH.; Wright, AC.; Wehrli, FW. Quantification of bound and mobile water in human cortical bone by ^{1}H and ^{2}H magnetic resonance. Proceedings of the 18th Annual Meeting ISMRM; Stockholm, Sweden. 2010. p. 799
31. Horch, RA.; Nyman, JS.; Gochberg, DF.; Does, MD. Correlation of ^{1}H NMR characteristics and mechanical properties in human cortical bone. Proceedings of the 18th Annual Meeting ISMRM; Stockholm, Sweden. 2010. p. 541

NIH-PA Author Manuscript

NIH-PA Author Manuscript

NIH-PA Author Manuscript

32. Roschger P, Rinnerthaler S, Yates J, Rodan GA, Fratzl P, Klaushofer K. Alendronate increases degree and uniformity of mineralization in cancellous bone and decreases the porosity in cortical bone of osteoporotic women. Bone. 2001; 29(2):185–191. [PubMed: 11502482]

33. Hopper TA, Wehrli FW, Saha PK, Andre JB, Wright AC, Sanchez CP, Leonard MB. Quantitative microcomputed tomography assessment of intratrabecular, intertrabecular, and cortical bone architecture in a rat model of severe renal osteodystrophy. J Comput Assist Tomogr. 2007; 31(2): 320–328. [PubMed: 17414773]

34. Laval-Jeantet AM, Bergot C, Carroll R, Garcia-Schaefer F. Cortical bone senescence and mineral bone density of the humerus. Calcif Tissue Int. 1983; 35:268–272. [PubMed: 6871757]

35. Bousson V, Bergot C, Meunier A, Barbot F, Parlier-Cuau C, Laval-Jeantet AM, Laredo JD. CT of the middiaphyseal femur: cortical bone mineral density and relation to porosity. Radiology. 2000; 217(1):179–187. [PubMed: 11012442]

36. Bousson V, Peyrin F, Bergot C, Hausard M, Sautet A, Laredo JD. Cortical bone in the human femoral neck: three-dimensional appearance and porosity using synchrotron radiation. J Bone Miner Res. 2004; 19(5):794–801. [PubMed: 15068503]

NIH-PA Author Manuscript
NIH-PA Author Manuscript
NIH-PA Author Manuscript

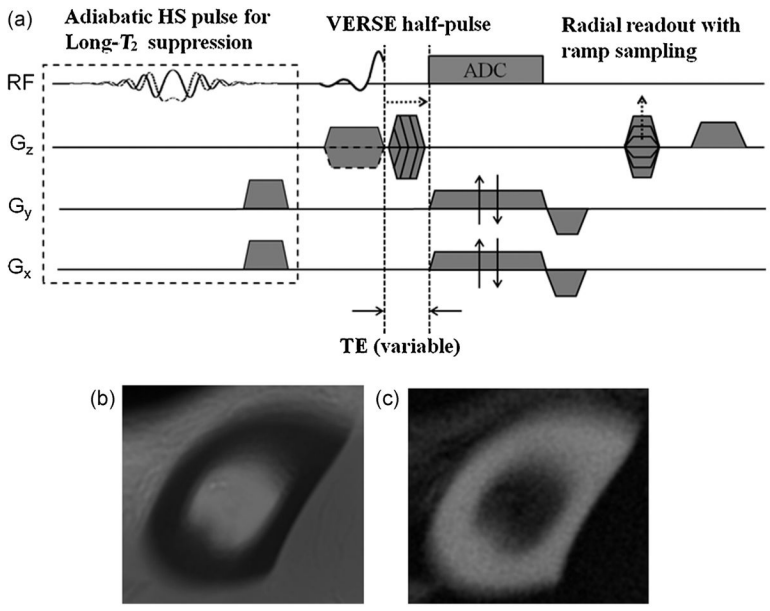

Figure 1.

(a) Schematic representation of three-dimensional hybrid-radial ultra-short echo-time (3D HRUTE) sequence with optional long-T_2 suppression pulse (based on dual-band spectrally selective pulses) utilizing pairs of half-sinc (HS) pulses for slab selection, radial readout with ramp sampling for k_x and k_y axes and variable-TE on the k_z axis to achieve minimal TE for $k_z = 0$. Sample 3D-HRUTE images of cortical bone acquired at 3-T field strength without (b) and with (c) soft-tissue suppression using an adiabatic hyperbolic secant pulse [pulse duration, 25 ms; excitation bandwidth, 800 Hz (centered at −270 Hz from the water peak); IR time for inversion recovery, 95 ms].

NIH-PA Author Manuscript

NIH-PA Author Manuscript

NIH-PA Author Manuscript

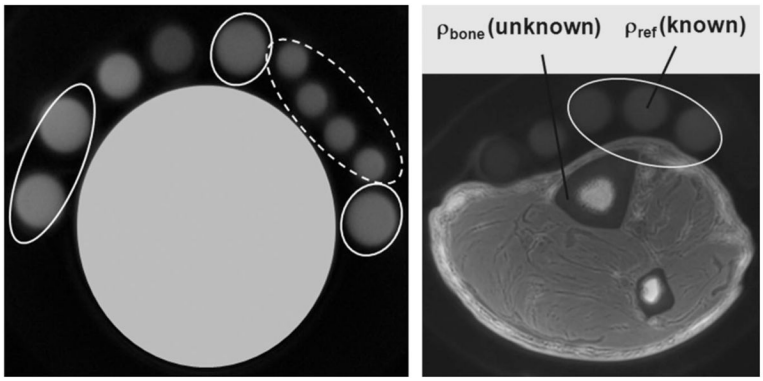

Figure 2.

(a) Phantom data from reference samples (20% H_2O in D_2O doped with 27 mM $MnCl_2$, yielding T_1 ~ 15 ms and T_2^* ~ 320 μs), showing the effect of receive coil inhomogeneity correction in two groups of reference samples; broken line, close mutual proximity; full line, dispersed in different locations. The ratio of the average signal divided by the standard deviation within each group increases substantially after correction: from 15.15 to 32.47 (broken line), and from 7.37 to 32.15 (full line). (b) Three-dimensional hybrid-radial ultra-short echo-time (3D-HRUTE) image (center slice) of tibial mid-shaft with reference samples. This image is corrected for the receive coil shading effect.

NIH-PA Author Manuscript

NIH-PA Author Manuscript

NIH-PA Author Manuscript

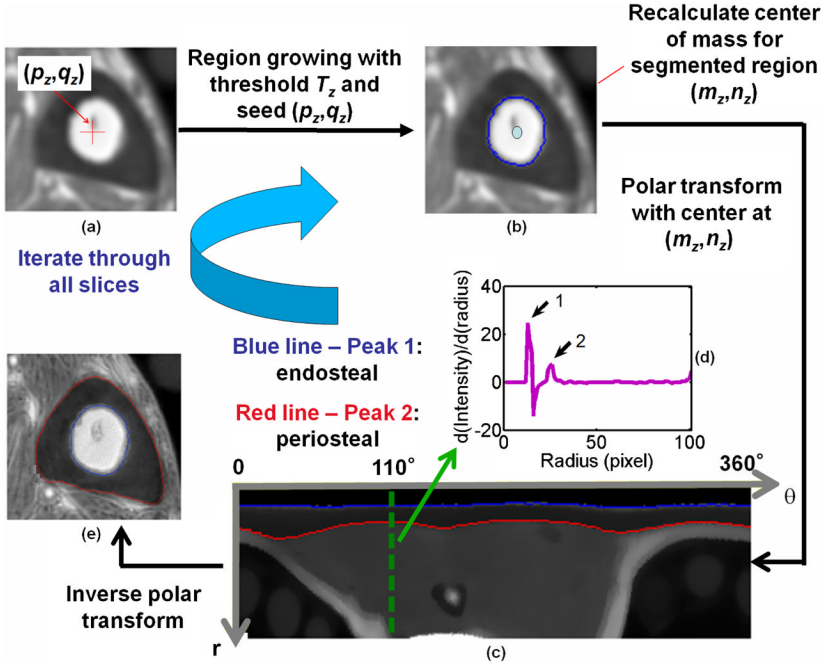

Figure 3.

Steps of automatic segmentation of cortical bone. (a, b) The bone marrow area is detected via a region growing algorithm with a dynamically calculated threshold (T_Z) based on the standard deviation of the intensity within a region around the initialization point (p_Z,q_Z), located by the user for slice $z = 1$ or automatically determined by finding the closest geodesic distance and intensity value compared with the center of mass of the previous slice ($m_Z - 1$,$n_Z - 1$) for $z > 1$. (c) Based on the segmentation mask, (m_Z,n_Z) is recalculated and taken as the center for two-dimensional polar image transform. (d) Intensity profile along the radius with respect to each degree. The first and second peaks of the derivative correspond to the endosteal and periosteal boundary (EB and PB) locations at each angular location. The purple line (inset) shows the derivative of the intensity profile along the radius at angular position $\theta = 110°$ with peaks 1 and 2 pertaining to EB and PB. (e) Inverse polar transform of these boundaries into Cartesian coordinates yields the final segmentation boundaries (blue and red).

NIH-PA Author Manuscript

NIH-PA Author Manuscript

NIH-PA Author Manuscript

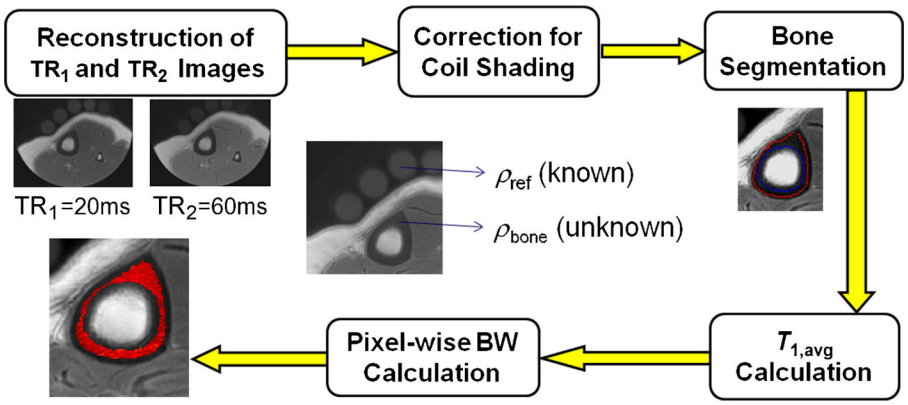

Figure 4.
Image analysis and bone water concentration (BWC) quantification flow diagram for human study.

NIH-PA Author Manuscript

NIH-PA Author Manuscript

NIH-PA Author Manuscript

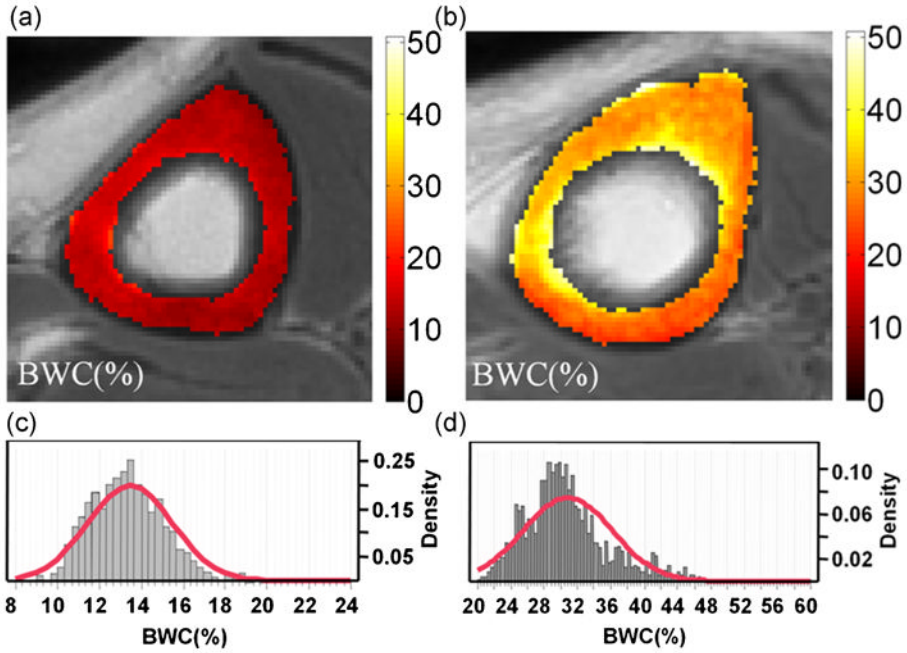

Figure 5.

Bone water concentration (BWC) map (%) images, together with their histograms and Gaussian-fitted curves in the central slice (10), for two subjects: (a, c) female, 33 years, $T_{1,avg}$ = 93.1 ms, BWC = 13.5 ± 2.0%; (b, d) female, 64 years, $T_{1,avg}$ = 270 ms, BWC = 38.8 ± 5.4%.

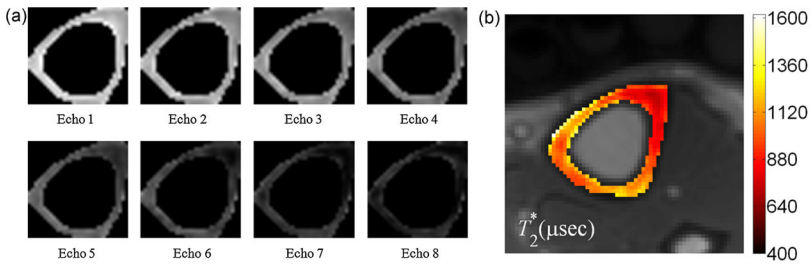

Figure 6.

(a) Segmented amplitude images of cortical bone at the tibial mid-shaft as a function of echo-time in a 53-year-old man. The echo-time spans the range 250–1650 μs in equal increments of 200 μs; (b) parametric T_2^* map superimposed on the anatomic image (mean and standard deviation, 840 ± 230 μs).

NIH-PA Author Manuscript
NIH-PA Author Manuscript
NIH-PA Author Manuscript

NIH-PA Author Manuscript

NIH-PA Author Manuscript

NIH-PA Author Manuscript

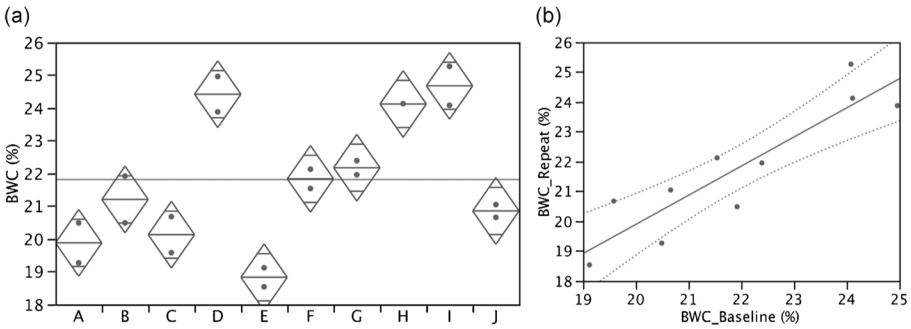

Figure 7.

Reproducibility data presented in scatter plot (a) and test–retest format (b). Data indicate root-mean-square difference (test–retest) of 0.914% bone water concentration (BWC) (4.2% relative to mean) and an intraclass correlation coefficient (ICC) of 0.95. Analysis of variance suggests significant differences among subjects ($p < 0.0001$).

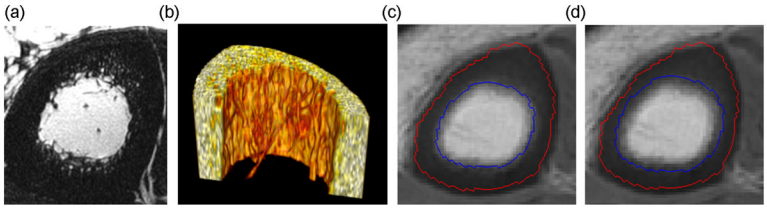

Figure 8.
High-resolution fast large-angle spin-echo (FLASE) images (137 × 137 μm^2) of the cortex in a 71-year-old woman: (a) two-dimensional image; (b) three-dimensional rendered image showing trabecularized endosteal boundary. Effects of marginIn on the endosteal boundary with fixed marginOut = 3: (c) marginIn = 2, bone water concentration (BWC) = 21.7%, T_1 = 157 ms; (d) marginIn = 4, BWC = 18.9%, T_1 = 137 ms.

NIH-PA Author Manuscript
NIH-PA Author Manuscript
NIH-PA Author Manuscript

NIH-PA Author Manuscript

NIH-PA Author Manuscript

NIH-PA Author Manuscript

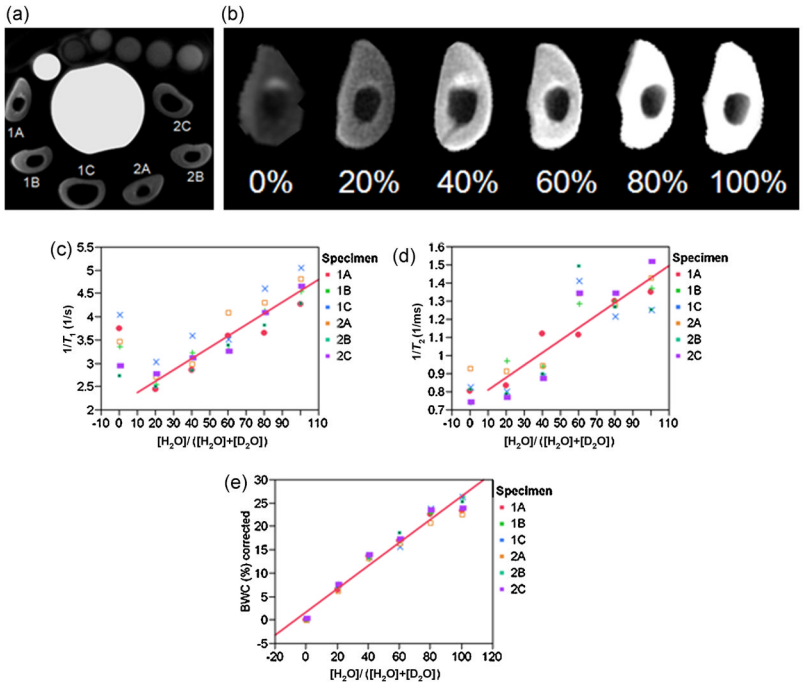

Figure 9.

Results of the specimen studies. (a) Imaging set-up showing the arrangement of six lamb tibia bone specimens surrounding a container of distilled water with reference samples on top, including an extra small tube filled with distilled water as a marker to allow consistent orientation. Images were obtained in air after removal from immersion fluid. Specimens from the two animals are labeled 1 and 2, with three contiguous sections (A–C). (b) Images from specimen 1A as a function of H_2O volume fraction, $[H_2O]/([H_2O] + [D_2O])$, of the immersion fluid. (c–e) $1/T_1$, $1/T_2^*$and bone water concentration (BWC), respectively, as a function of H_2O volume fraction, together with the linear fits after averaging the data over all six specimens: $1/T_1$, $R^2 = 0.87$; $1/T_2^*$, $R^2 = 0.70$; BWC, $R^2 = 0.95$.